Supporting information

Tuning valence-variable single atomic metal for efficient antibiotic degradation and in-situ chlorinated byproduct elimination under current pulsation

Yang Yu [a,c], Yibo Lin [a,c], Binyao Wang [a,c], Yangqi E [a,c], Qian Li [a,c], Huachang Jin [b], Raúl Muñoz Torre [d], Zhao Huang [e], Jianmeng Chen [f], Dongzhi Chen [a,c,*]

[a] *Zhejiang Key Laboratory of Pollution Control for Port-Petrochemical Industry, Zhejiang Ocean University, Zhoushan 316022, China*

[b] *National and Local Joint Engineering Research Center, College of Life and Environmental Science, Wenzhou University, Wenzhou 325035, China*

[c] *National & Local Joint Engineering Research Center of Harbor Oil & Gas Storage and Transportation Technology, Zhejiang Ocean University, Zhoushan 316022, China*

[d] *Institute of Sustainable Processes, University of Valladolid, Valladolid, 47011, Spain*

[e] *China National Offshore Oil Corporation Limited Shanghai Branch, Shanghai, 200051, China*

[f] *College of Environmental and Resources Science, Zhejiang University of Science & Technology, Hangzhou, 310032, China*

---

[*]Corresponding author email addresses: chendz@zjou.edu.cn (Dongzhi Chen).

Text S1. Chemicals.

$Rh(NO_3)_3$ (≥95.0%), $Mn(NO_3)_3$ (≥50.0%), tetracycline (≥98.0%), cephalexin (≥95.0%), cloxacillin (≥95.0%), levofloxacin (≥98.0%), sulfadiazine (≥98.0%), cephalosporin (≥90.0%), *p*-benzoquinone (*p*-BQ, ≥99.0%), L-histidine (≥99.0%), urea (≥99.0%), dimethyl sulfoxide (DMSO, ≥99.0%), I_2 (≥99.8%), *p*-chlorobenzoic acid (*p*CBA, ≥99.8%), furfuryl alcohol (FFA, ≥98.0%), and methyl phenyl sulfoxide (PMSO, ≥97.0%) were purchased from Aladdin Reagent Inc., China. Potassium ferricyanide ($K_3[Fe(CN)_6]$, ≥99.5%) and potassium ferrocyanide ($K_4[Fe(CN)_6]$, ≥98.0%) were purchased from Macklin Reagent Co., Ltd., China. Oxalic acid (≥99.5%), benzoic acid (BA, ≥99.5%), formic acid (HPLC), acetonitrile (HPLC), methyl tert butyl ether (≥99.0%), isopropanol (≥99.7%), hydrochloric acid (HCl, ≥36.0%), sodium hydroxide (NaOH, ≥96.0%), sulfuric acid (H_2SO_4, 95.0%~98.0%), sodium chloride (NaCl, ≥99.5%), sodium sulfate (Na_2SO_4, ≥99.0%), potassium sulfate (K_2SO_4, ≥99.0%), *tert* butanol alcohol (TBA, ≥99.0%), and $K_2Cr_2O_7$ (≥99.8%) were purchased from Sinopharm Chemical Reagent Co., Ltd., China.

Text S2. Detailed procedures of electrochemical characterization.

Cyclic voltammetry (CV): To assess the oxygen/chlorine evolution, conventional CV was performed in 0.5 M H_2SO_4 and 0.5 M NaCl at a scan rate of 100 $mV \cdot s^{-1}$. To probe the pseudocapacitive behavior, redox CV with the stepwise decreased potential limits was performed in 0.5 M H_2SO_4 at a scan rate of 100 $mV \cdot s^{-1}$. To examine the reversibility of the interfacial electron transfer between electrode and electrolyte, CV

was performed in 10 mM $[Fe(CN)_6]^{3-/4-}$at a scan rate of 100 $mV \cdot s^{-1}$.

Tafel polarization: Tafel polarization was derived from the conventional CV.

Electrochemical impedance spectroscopy (EIS): EIS was performed in 0.5 M Na_2SO_4 with an applied bias of 0.5 V and a sinus amplitude of 10 mV over a frequency range of 10^5 to 10 Hz. Nyquist plots were fitted with an equivalent circuit model using the Zview software.

Charging-discharging: Charging-discharging was performed in pulsed voltage or current. For pulsed voltage, -1 V and 1 V voltage were applied to alternately charge and discharge the electrode, and the corresponding current change was monitored. The total charges transferred during the charging and discharging stages were calculated as follows:

$$Q_{c,charging} = \int_0^x (I_{charging} - I_{end})dt \quad \text{(S1)}$$

$$Q_{c,discharging} = \int_0^x (I_{discharging} - I_{end})dt \quad \text{(S2)}$$

where $Q_{c,charging}$ and $Q_{c,discharging}$ are capacitive charges transferred during the charging and discharging stages, C; $I_{charging}$ and $I_{discharging}$ are instantaneous currents during the charging and discharging stages, A; I_{end} is the end current during the charging and discharging stages, A; t is the time, s. For pulsed current, 0.1 A and 0 A were applied to alternately charge and discharge the electrode, and the corresponding voltage change was monitored. The specific capacitance could then be calculated as follows:

$$SC = \frac{I\Delta t}{S\Delta E} \quad \text{(S3)}$$

where I is the current, A; ΔE is the potential change, V; S is the electrode area, m^2.

Accelerated life test: Service life evaluation is time-consuming in normal conditions. To save experiment time, the accelerated life test was conducted under harsh conditions, *i.e.*, overly high current densities and very short pulsation periods. During the accelerated life test, the pulsation period was automatically controlled via a programmable controller, and a constant current density of 1000-5000 $A \cdot m^{-2}$ and a pulsation period of 2.5-30 min was applied to the electrode. The accelerated service life was defined as working hours at which the voltage variation exceeded 5 V.

Text S3. Details of automatic control strategy for anode-cathode pulsation.

The automatic control of anode-cathode pulsation was implemented via a programmable logic relay (PLR). This system was programmed to execute precise timing sequences that alternately trigger the anode and cathode circuits through its digital output channels. The PLR's internal clock synchronized switching operations between the two electrodes, enabling fully automated pulsation cycles without manual intervention. Real-time monitoring via the relay's interface ensured operational stability throughout experiments.

Square-wave potentials were applied to the electrodes, with the anode potential cycling between +1 V and +5 V and the cathode potential cycling between -1 V and -5 V. The polarity ratio was adjustable within the range of 10:1 to 1:1, and the frequency was set between 72 d^{-1} and 720 d^{-1}.

Text S4. Details of response surface methodology (RSM).

Design-Expert.V13.0 software was used to establish RSM, wherein Box-Behnken Design method was taken into consideration. Current density, pulsation frequency, and NaCl concentration were set as independent variables, while tetracycline removal and byproduct concentration were set as dependent variables. The arrangements of the experiment are listed in Table S2.

Text S5. Detailed procedures of analysis.

Antibiotic quantification: Antibiotics were quantified using a high-performance liquid chromatograph (HPLC, 1260, Agilent, USA) equipped with a C18 column and a UV detector. The mobile phase was the mixture of acetonitrile and 0.1% formic acid (v/v=60/40) at a flow rate of 1 $mL \cdot min^{-1}$, and the wavelength detection range was 200-400 nm depending on the detection limit of each antibiotic.

Carboxylic acid and inorganic chlorinated byproduct quantification: Carboxylic acids and inorganic chlorinated byproducts (ClO_3^- and ClO_4^-) were quantified using an ion chromatograph (IC, Aquion RFIC, Dionex, USA) equipped with an IonPac AG19 guard column and an electron conductivity detector. Before analysis, the sample was diluted with deionized water, and then filtered through a 0.22 μm filter. The eluent was KOH, which flowed at a constant flow rate of 1 $mL \cdot min^{-1}$.

Organic chlorinated byproduct quantification: Organic chlorinated byproducts (chloroacetic acids and chloromethanes) were quantified by a gas chromatograph and a tandem mass spectrometer (GC-MS, GC7890B-MS5977B, Agilent, USA) equipped

with a DB-VRX column. For chloroacetic acids, the sample followed emendation with Na_2SO_4, acidification (1 ml H_2SO_4), extraction (methyl tert butyl ether), esterification with 1 ml methanol and 10% H_2SO_4, rinsing with 10% Na_2SO_4, and then directly quantification with GC-MS. The temperature of the injector was 220°C, while the temperature program of the oven was set as follows: 35°C (held for 10 min), a ramp of 5°C·min^{-1} to 75°C (held for 15 min), a ramp of 40°C·min^{-1} to 185°C (held for 5 min). He was supplied as the carrier gas, and the sample injection volume, split ratio, and column flow rate were maintained at 1 uL, 20:1, and 2 mL·min^{-1}. For chloromethanes, the sample was concentrated using the purge-trap method, and then directly quantified by GC-MS. The temperature of the injector was 220°C, while the temperature program of the oven was set as follows: 35°C (held for 5 min), a ramp of 6°C·min^{-1} to 100°C (held for 2 min), a ramp of 20°C·min^{-1} to 210°C (held for 1 min). He was supplied as the carrier gas, and the split ratio and column flow rate were maintained at 20:1 and 2 mL·min^{-1}. The mass spectrometer equipped with an electron impact ion source was run in full scan mode. The ionization mass spectra were acquired at the ionization energy of 70 eV and an ionization source temperature of 230°C.

Aromatic compound identification: Aromatic compounds were identified by a liquid chromatograph and a tandem mass spectrometer (LC-MS, 1290-6550qtof, Agilent, USA). The liquid chromatograph was equipped with a C18 column, and the mobile phase was the mixture of acetonitrile and 0.1% formic acid (v/v=60/40) at a flow rate of 1 mL·min^{-1}. The mass spectrometer equipped with an electron impact ion

source was run in full scan mode. Finally, the possible aromatic compounds were inferred using the NIST library.

Toxicity assessment: Toxicity of degradation intermediates was conducted using a toxicity estimation software tool, wherein the daphnia magna lethal concentration 50 (LC_{50}) and bioconcentration factor were used as the indicators.

Text S6. The details of density functional theory (DFT).

Vienna Ab Initio Package was used to develop the DFT calculation. The electron exchange and correlation energies were handled with the Perdew-Burke-Ernzerhof in the generalized gradient approximation. The coactions between the valence electrons and ionic cores were implemented using the projector augmented wave function. The Monk-horst-Pack Γ centered grids were used for the structure optimization, and the slab relaxations were carried out with a 400 eV plane-wave cut-off energy. The climbing image nudged elastic band method was employed to calculate the energy barrier for oxygen evolution and RCS production. The convergence criteria of structure optimization and transition states for force per atom were set to 0.02 and 0.05 $eV \cdot Å^{-1}$, and for energy were set to 10^{-5} and 10^{-7} eV, respectively. Three models, Mn-SA, Rh-SA, and Rh/Mn-SAH were established by *ab initio* molecular dynamics. The nudged elastic band was used to verify the energy steps of the oxygen evolution reaction and RCS production.

Text S7. Calculations of the energy consumption and current efficiency.

The energy consumption and current efficiency were calculated according to the following equations [1]:

$$\text{Energy consumption} = \frac{UI}{V\left(COD_0 - COD_t\right)} \tag{S4}$$

$$\text{Current efficiency} = \frac{V\left(COD_0 - COD_t\right)}{8 \times 60 \times It/F} \times 100\% \tag{S5}$$

where U is the applied voltage, V; I is the applied current, A; COD_0 and COD_t are the chemical oxygen demand at 0 min and t min, respectively, $g \cdot L^{-1}$; F is the Faraday constant, 96485 $C \cdot mol^{-1}$; V is the volume of treated wastewater, L; 8 represents the corresponding electron transfer number per molecule of O_2; 60 is conversion coefficients.

Text S8. Calculations of the pseudo-first-order reaction rate constants (k_{obs}) that normalized with electrochemical surface area (ESCA) and treated solution volume.

The k_{obs} was calculated according to [2]:

$$-\ln\frac{[pollutant]}{[pollutant]_0} = k_{obs,Pollutant}t \tag{S6}$$

where pollutant and $pollutant_0$ are instantaneous and initial concentrations of pollutant, $mg \cdot L^{-1}$; t is the treatment time, s.

ESCA was obtained from CV plots in Figure S12 using the following equation:

$$ESCA = \frac{C_{dl} \times A}{C_s} \tag{S7}$$

where C_{dl} is the tested double-layer capacitance from CV, $mF \cdot cm^{-2}$; Cs is the average double-layer capacitance of electrodes, 0.06 $mF \cdot cm^{-2}$; A is the geometrical area of the

tested electrode, m^2. Then, the normalized k_{obs} could be calculated according to [3]:

$$\text{Normalized } k\text{obs} = \frac{V \times k\text{obs}}{\text{ESCA}} \quad \text{(S8)}$$

where V is the volume of the treated solution, m^3.

Text S9. Detailed calculation of the chemical probing test.

Oxalic acid (OA), benzoic acid (BA), *p*-chlorobenzoic acid (*p*CBA), furfuryl alcohol (FFA), urea, and methyl phenyl sulfoxide (PMSO) were used as the probe compounds for direct electron transfer (DET), •OH, $\bullet O_2^-$, $^1O_2$, reactive chlorine species (RCS), and high-valent metal (M_{high}), respectively.

(1) k_{obs} between DET and tetracycline.

k_{obs} between DET and various pollutants were considered to be consistent, thus the K_{obs} between DET and OA was identical to the k_{obs} between DET and tetracycline, as expressed as follows:

$$-\ln\frac{[OA]}{[OA]_0} = k_{obs,OA}t = k_{obs,tetracycline,DET}t \quad \text{(S9)}$$

where OA and OA_0 are instantaneous and initial concentrations of OA, respectively, $mg \cdot L^{-1}$; t is the treatment time, s; $k_{obs,OA}$ and $k_{obs,tetracycline,DET}$ are pseudo-first-order reaction rate constants between DET and OA and between DET and tetracycline, respectively, which are identical and can be obtained from the plots of $-\ln\frac{[OA]}{[OA]_0}$ versus time (Figures S18a-S18d).

(2) The steady-state concentrations of •OH, $\bullet O_2^-$, $^1O_2$, and RCS.

$$-\frac{d[BA]}{dt} = k_{BA,\bullet OH}[\bullet OH][BA] \quad \text{(S10)}$$

$$-\frac{d[p\text{CBA}]}{dt} = k_{p\text{CBA},\bullet OH}[\bullet OH][p\text{CBA}] + k_{p\text{CBA},\bullet O_2^-}\left[\bullet O_2^-\right][p\text{CBA}] + k_{p\text{CBA},1O2}[1O2][p\text{CBA}] \quad \text{(S11)}$$

$$-\frac{d[FFA]}{dt} = k_{FFA,\bullet OH}[\bullet OH][FFA] + k_{FFA,\bullet O_2^-}\left[\bullet O_2^-\right][FFA] + k_{FFA,1O_2}[1O2][FFA] \quad \text{(S12)}$$

$$-\frac{d[urea]}{dt} = k_{urea,RCS}[RCS][urea] \quad \text{(S13)}$$

where $k_{BA,\bullet OH}$, $k_{p\text{CBA},\bullet OH}$, $k_{p\text{CBA},\bullet O_2^-}$, $k_{p\text{CBA},1O2}$, $k_{FFA,\bullet OH}$, $k_{FFA,\bullet O_2^-}$, $k_{FFA,1O_2}$, $k_{urea,RCS}$ the second-order reaction rate constants between probe compounds and oxidative species, as shown in Table S5. Integrating Equations S10-S13, then above equations could be rewritten as:

$$-\ln\frac{[BA]}{[BA]_0} = \left(k_{BA,\bullet OH}[\bullet OH]_{ss}\right)t = k_{obs,BA}t \quad \text{(S14)}$$

$$-\ln\frac{[p\text{CBA}]}{[p\text{CBA}]_0} = \left(k_{p\text{CBA},\bullet OH}[\bullet OH]_{ss} + k_{p\text{CBA},\bullet O_2^-}\left[\bullet O_2^-\right]_{ss} + k_{p\text{CBA},1O2}[1O2]_{ss}\right)t = k_{obs,p\text{CBA}}t \quad \text{(S15)}$$

$$-\ln\frac{[FFA]}{[FFA]_0} = \left(k_{FFA,\bullet OH}[\bullet OH]_{SS} + k_{FFA,\bullet O_2^-}\left[\bullet O_2^-\right]_{SS} + k_{FFA,1O2}[1O2]_{SS}\right)t = k_{obs,FFA}t \quad \text{(S16)}$$

$$-\ln\frac{[urea]}{[urea]_0} = \left(k_{urea,RCS}[RCS]_{ss}\right)t = k_{obs,urea}t \quad \text{(S17)}$$

where BA/BA_0, pCBA/pCBA_0, FFA/FFA_0, and urea/$urea_0$ are instantaneous/initial

concentrations of probe compounds, respectively, $mg \cdot L^{-1}$; t is the treatment time, s; $[\bullet OH]_{SS}$, $[\bullet O_2^-]_{SS}$, $[^1O_2]_{SS}$, and $[RCS]_{SS}$ are the steady-state concentrations of •OH, $\bullet O_2^-$, $^1O_2$, and RCS, respectively, M; $k_{obs,BA}$, $k_{obs,pCBA}$, $k_{obs,FFA}$, and $k_{obs,urea}$ are the pseudo-first-order reaction rate constants between BA/*p*CBA/FFA/urea and oxidative species, which can be obtained from the plots of $-\ln\frac{[BA]}{[BA]_0}$, $-\ln\frac{[pCBA]}{[pCBA]_0}$, $-\ln\frac{[FFA]}{[FFA]_0}$, and $-\ln\frac{[urea]}{[urea]_0}$ versus time, respectively (Figures S18a-S18d). Then, $[\bullet OH]_{SS}$, $[\bullet O_2^-]_{SS}$, $[^1O_2]_{SS}$, and $[RCS]_{SS}$ can be obtained by solving Equations S14-S17.

(3) The steady-state concentration of M_{high}.

$$-\frac{d[PMSO_2]}{dt} = k_{PMSO,M_{high}}[M_{high}][PMSO] \quad (S18)$$

$$\eta = \frac{\Delta[PMSO_2]}{\Delta[PMSO]} = \frac{[PMSO_2]}{[PMSO]_0 - [PMSO]} \quad (S19)$$

where η is the conversion rate of PMSO, which means mole of $PMSO_2$ produced per mole of PMSO oxidized, which can be obtained from Figure S18e. Combing Equation S18 with Equation S19, the above equation could be written as:

$$\frac{d[PMSO_2]}{[PMSO]_0 - \frac{1}{\eta}[PMSO_2]} = \frac{d[PMSO_2]}{[PMSO]} = -k_{PMSO,M_{high}}[M_{high}]dt \quad (S20)$$

Integrating Equation S20, then the above equation could be rewritten as:

$$\eta\ln\frac{[PMSO]_0}{[PMSO]_0 - \frac{1}{\eta}[PMSO_2]} = -\eta\ln\frac{[PMSO]}{[PMSO]_0} = k_{PMSO,M_{high}}[M_{high}]_{ss}t$$

$$= \eta k_{obs,PMSO}t \quad (S21)$$

where $k_{obs,PMSO}$ is the pseudo-first-order reaction rate constants between PMSO and

M_{high}, which can be obtained from the plots of $-\ln\frac{[PMSO]}{[PMSO]_0}$ versus time, respectively (Figures S18a-S18c); t is the treatment time, s. Then, $[M_{high}]_{SS}$ can be obtained by solving Equation S21.

Text S10. Regression equations relating tetracycline removal (Y_1) and chlorinated byproduct concentration (Y_2) to current density (X_1), pulsation frequency (X_2) and NaCl concentration (X_3)

$$Y_1=83.06+4.84X_1-7.14X_2+6.12X_3+2.38X_1X_2+0.125X_1X_3+0.0369X_2X_3-3.01X_1^2-0.2725X_2^2+2.73X_3^2 \quad (S30)$$

$$Y_2=0.2502+0.0078X_1+0.0923X_2+0.0417X_3+0.0096X_1X_2+0.0008X_1X_3-0.0141X_2X_3-0.0209X_1^2+0.0142X_2^2+0.0214X_3^2 \quad (S31)$$

Text S11. The empirical model relating service life (SL) to current density (I) and pulsation period (P)

$$SL \propto (I)^{n_1}(P)^{n_2} \quad (S32)$$

where SL is service live, h; I is the current density, $A \cdot m^{-2}$; P is the pulsation period, min; n_1 and n_2 are coefficients, which are -1.9 and 0.3, respectively.

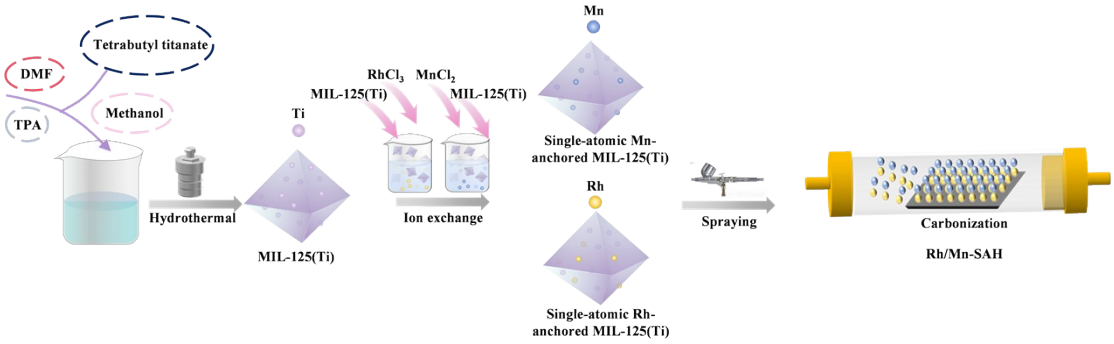

Figure S1. Schematic illustration of the Rh/Mn-SAH electrode synthesis procedure.

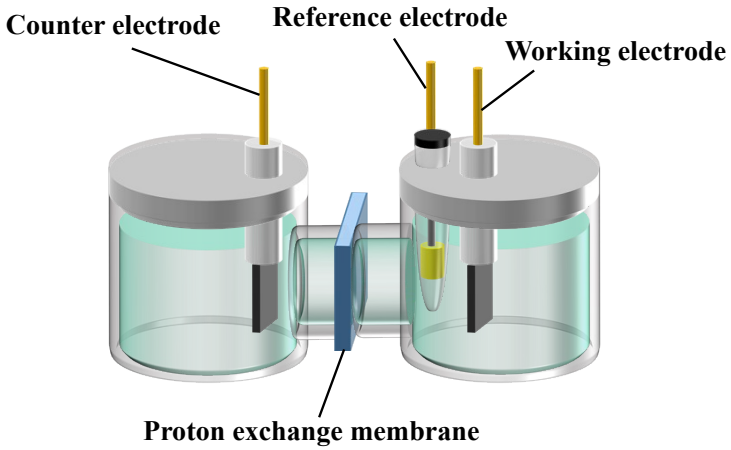

Figure S2. Schematic diagram of membrane-divided three-electrode system.

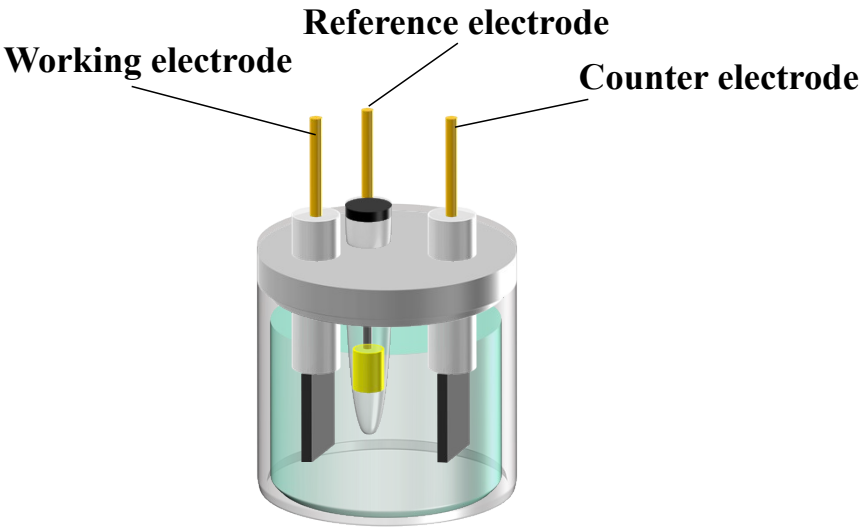

Figure S3. Schematic diagram of undivided three-electrode system.

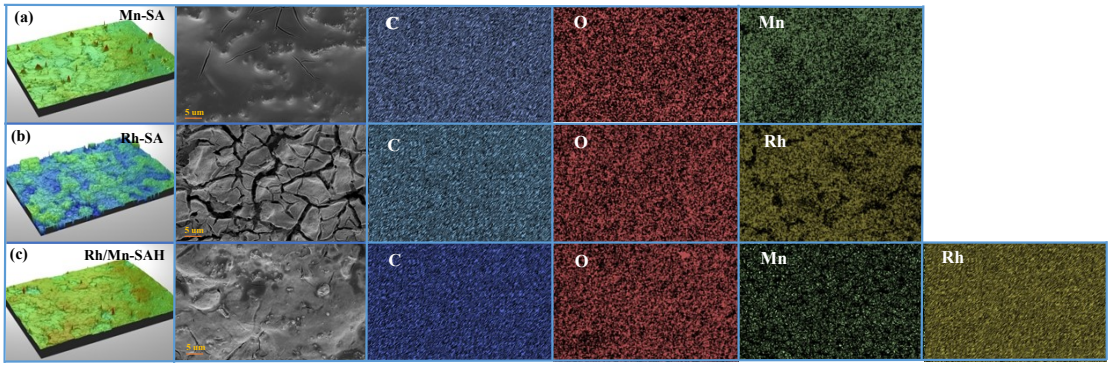

Figure S4. Three-dimensional pictures, two-dimensional pictures, and corresponding elemental mapping of (a) Mn-SA, (b) Rh-SA, and (c) Rh/Mn-SAH.

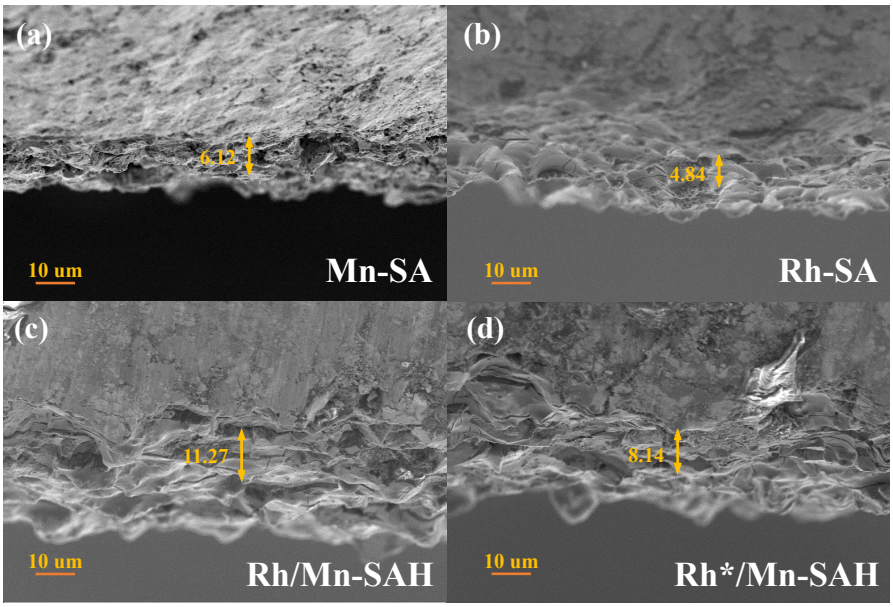

Figure S5. Thicknesses of (a) Mn-SA, (b) Rh-SA, (c) Rh/Mn-SAH, and (d) Rh*/Mn-SAH.

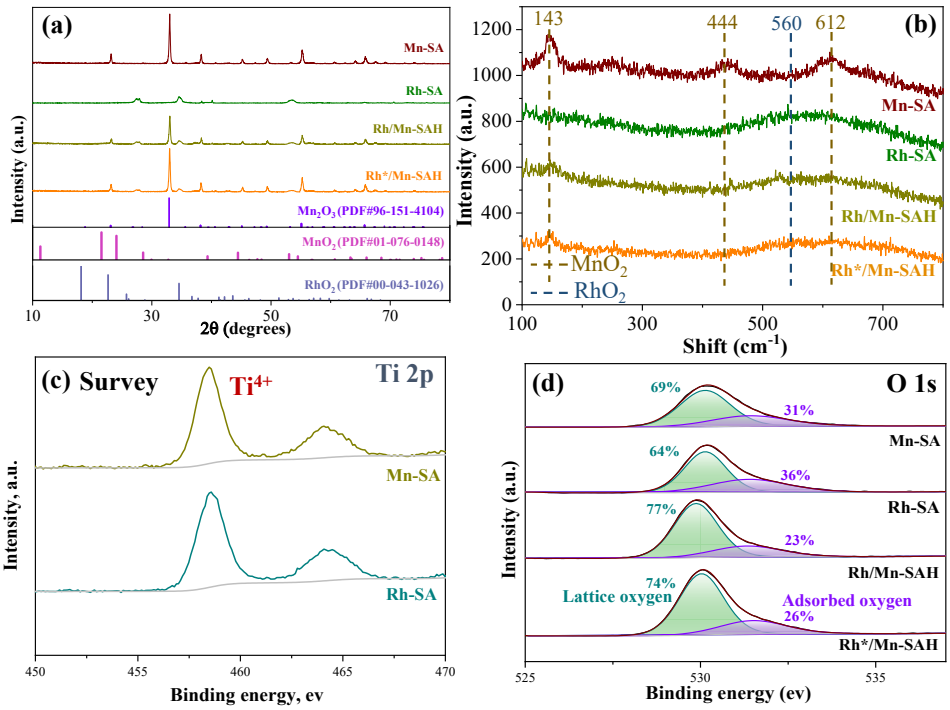

Figure S6. (a) XRD spectra, (b) Raman spectra, (c) Ti 2p, and (d) O 1s XPS spectra of different electrodes.

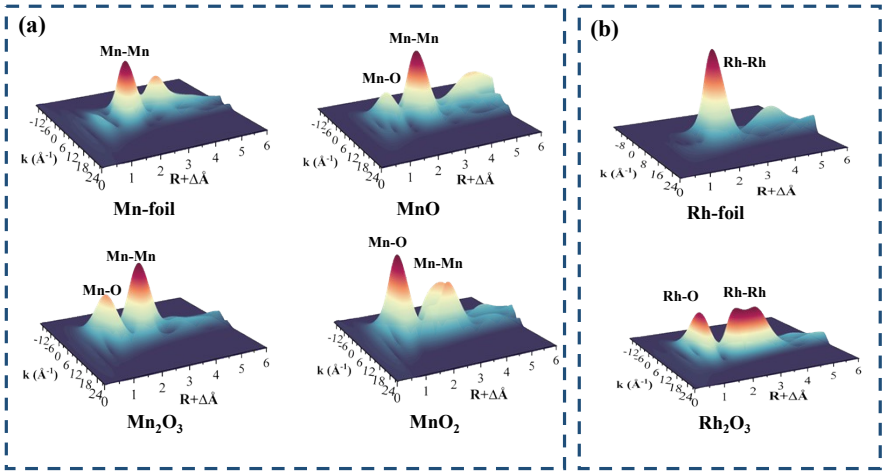

Figure S7. Wavelet transform analysis of (a) Mn-related standards and (b) Rh-related standards.

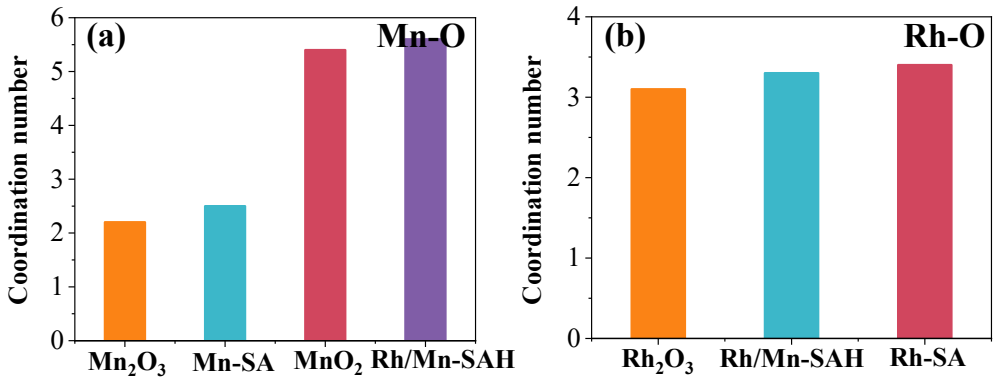

Figure S8. Coordination numbers for (a) Mn-O bond and (b) Rh-O bond obtained by EXAFS spectral curve fitting.

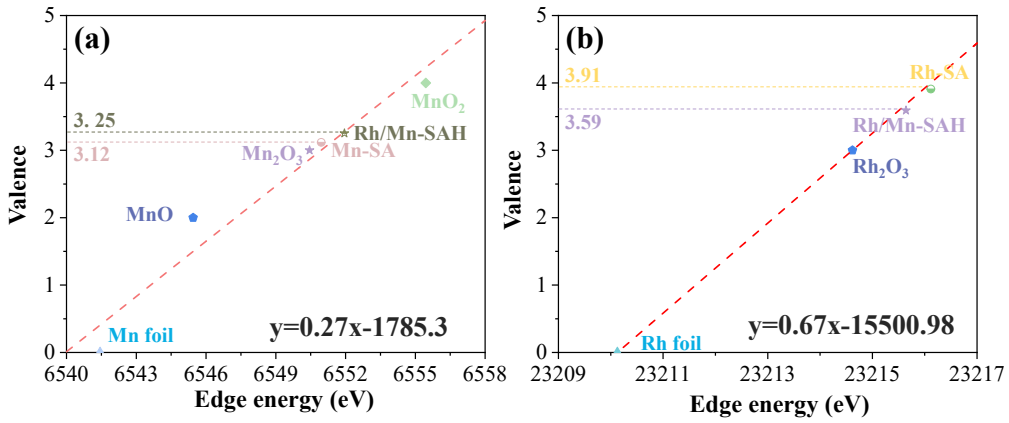

Figure S9. *K*-edge-valence correlation for (a) Mn and (b) Rh species.

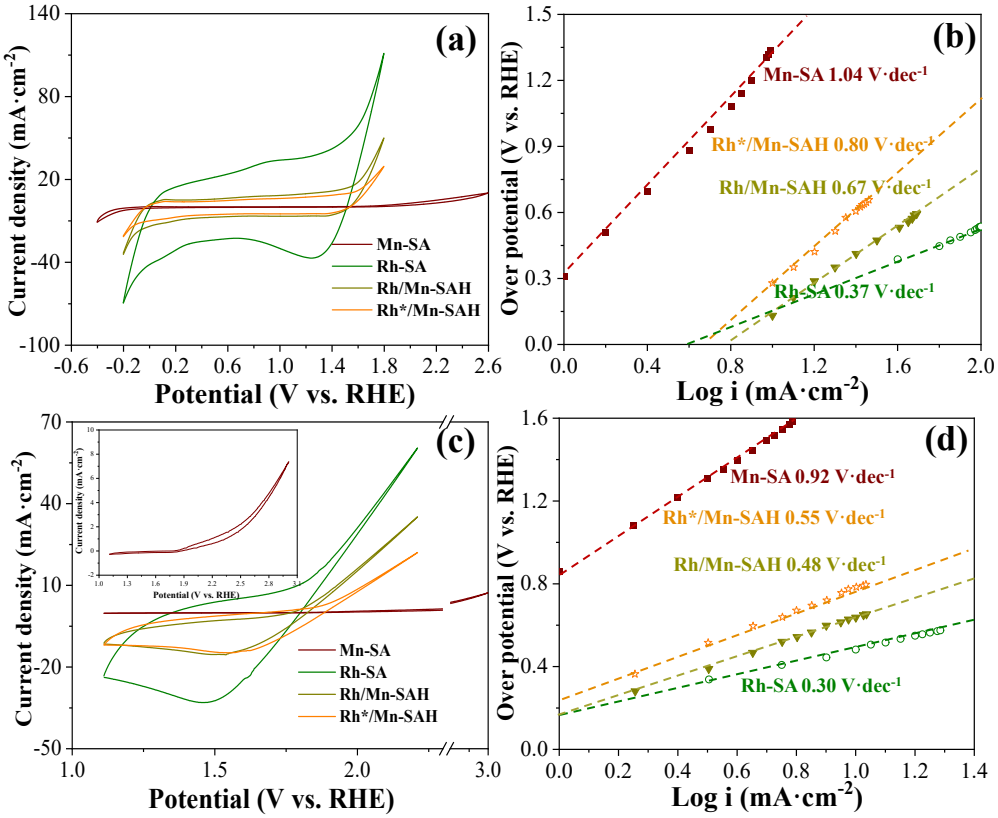

Figure S10. (a) CV for oxygen evolution and (b) corresponding Tafel plots. (c) CV for chlorine evolution and (d) corresponding Tafel plots.

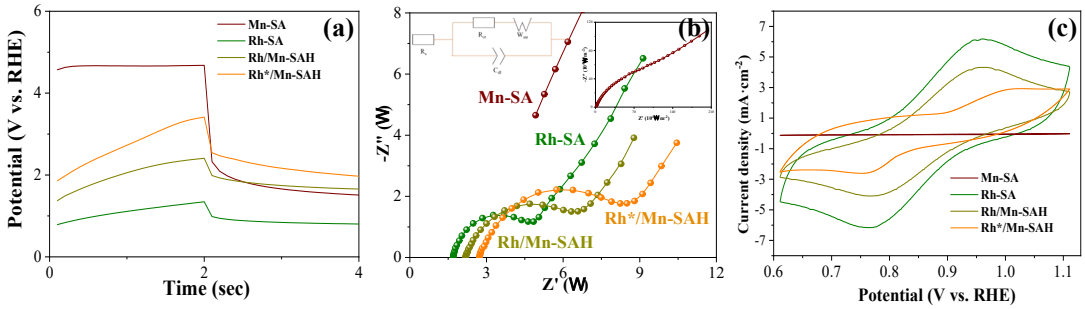

Figure S11. (a) Pulsed current-induced charge-discharge plots, (b) EIS plots, and (c) CV diagram in 10 mM $[Fe(CN)_6]^{3-/4-}$of Mn-SA, Rh-SA, Rh/Mn-SAH, and Rh*/Mn-SAH.

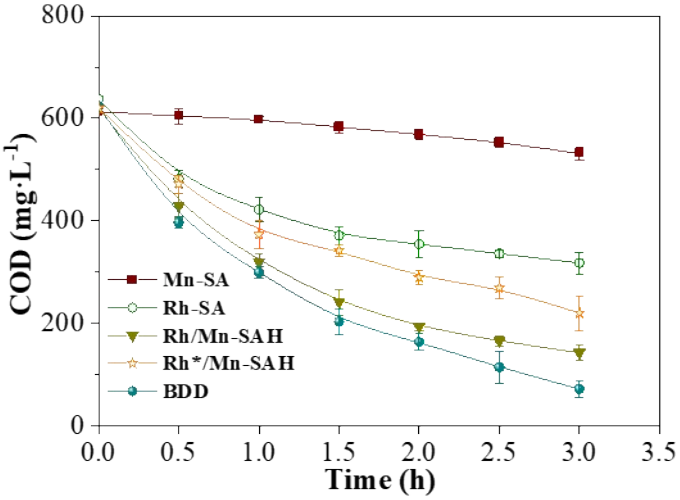

Figure S12. COD variations during electrocatalytic oxidation of tetracycline.

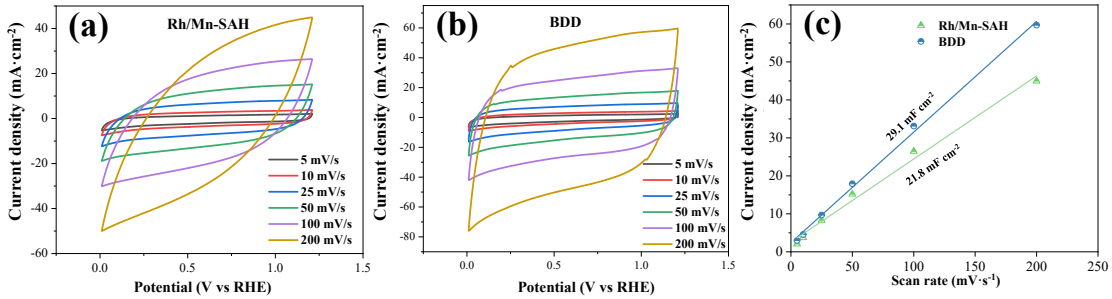

Figure S13. CV plots at different scan rates for (a) Rh/Mn-SAH and (b) BDD. (c) CV current as a function of scan rate.

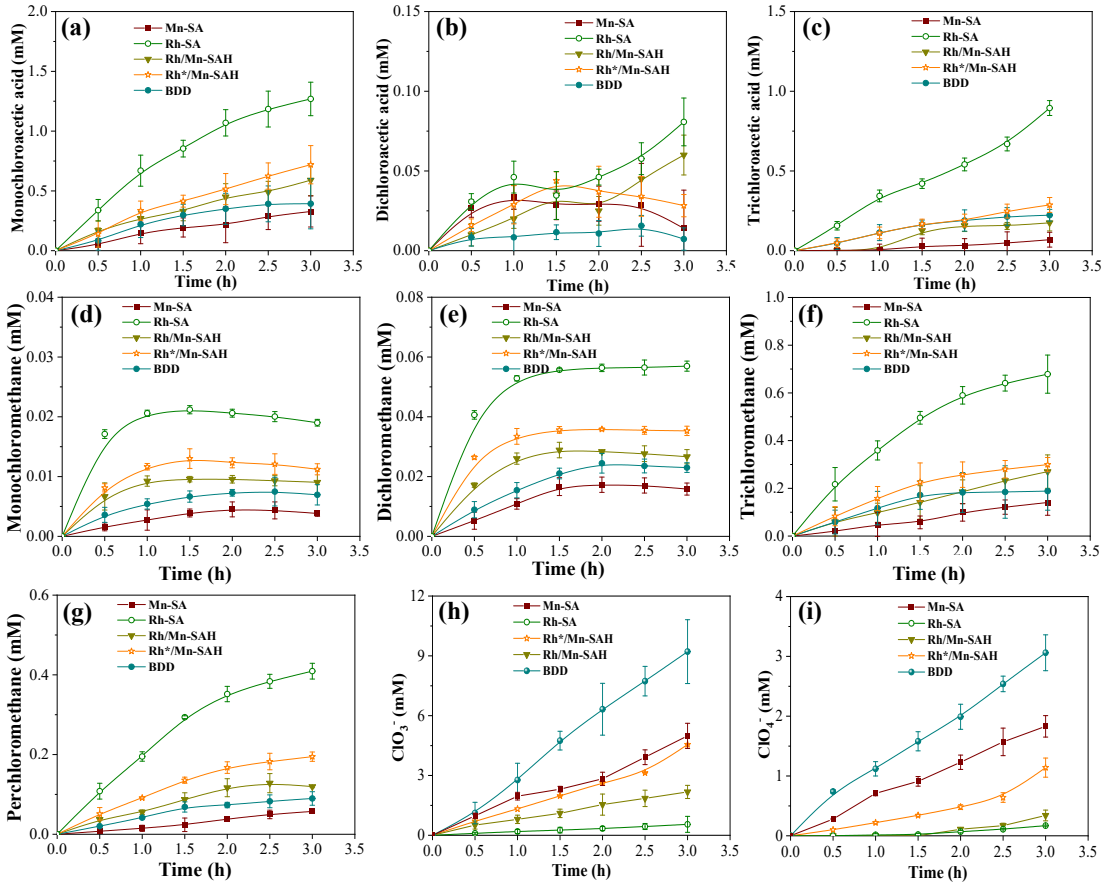

Figure S14. Chlorinated byproducts variations during electrocatalytic oxidation of tetracycline. (a) Monochloroacetic acid, (b) dichloroacetic acid, (c) trichloroacetic acid, (d) monochloromethane, (e) dichloromethane, (f) trichloromethane, (g) perchloromethane, (h) ClO_3^-, and (i) ClO_4^-. Experimental conditions: initial tetracycline concentration = 320 mg·L^{-1}, initial NaCl concentration = 60 mM, current density = 20 mA·cm^{-2}.

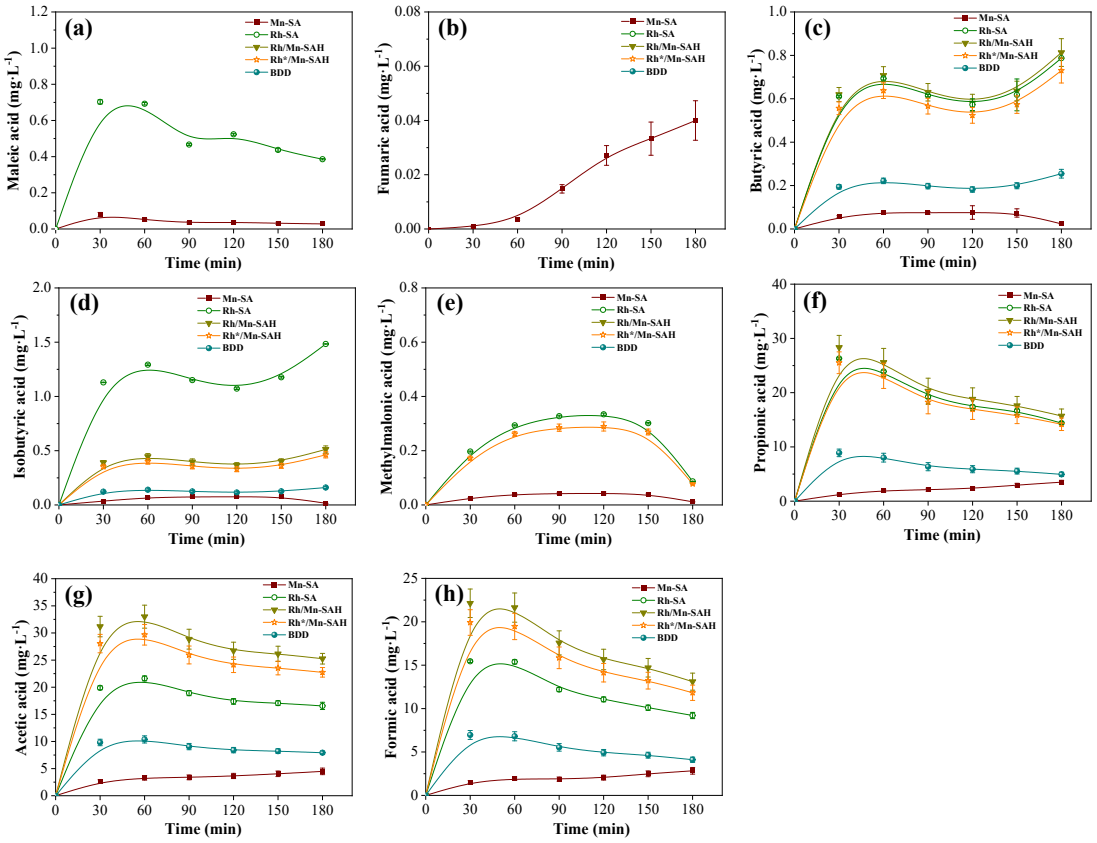

Figure S15. Carboxylic acids variations during electrocatalytic oxidation of tetracycline. (a) Maleic acid, (b) fumaric acid, (c) butyric acid, (d) isobutyric acid, (e) methylmalonic acid, (f) propionic acid, (g) acetic acid, and (d) formic acid. Experimental conditions: initial tetracycline concentration = 320 $mg \cdot L^{-1}$, initial NaCl concentration = 60 mM, current density = 20 $mA \cdot cm^{-2}$.

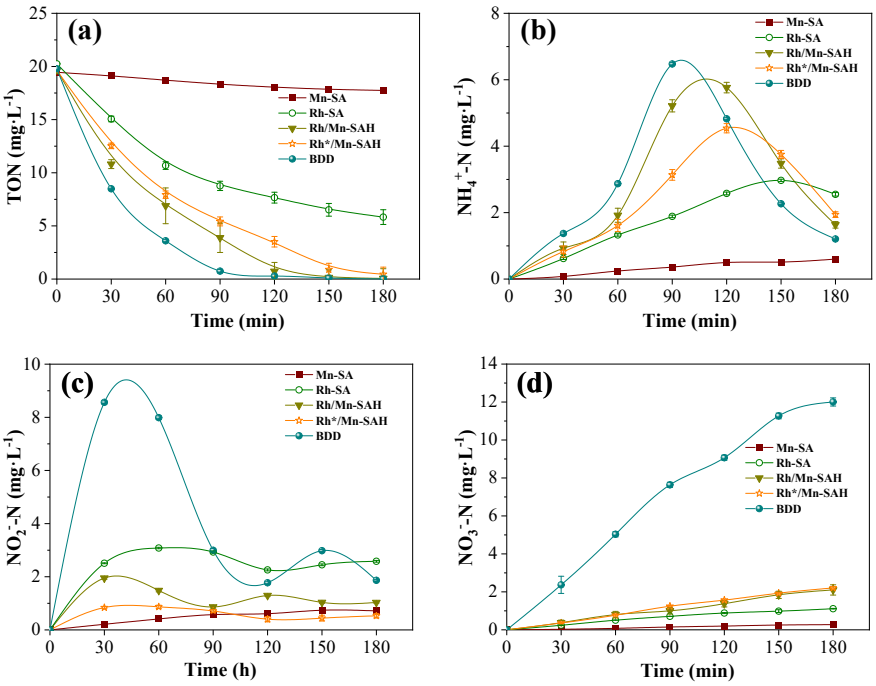

Figure S16. N-contained species variations during electrocatalytic oxidation of tetracycline. (a) TON, (b) NH_4^+-N, (c) NO_2^--N, and (d) NO_3^--N. Experimental conditions: initial tetracycline concentration = 320 mg·L^{-1}, initial NaCl concentration = 60 mM, current density = 20 mA·cm^{-2}.

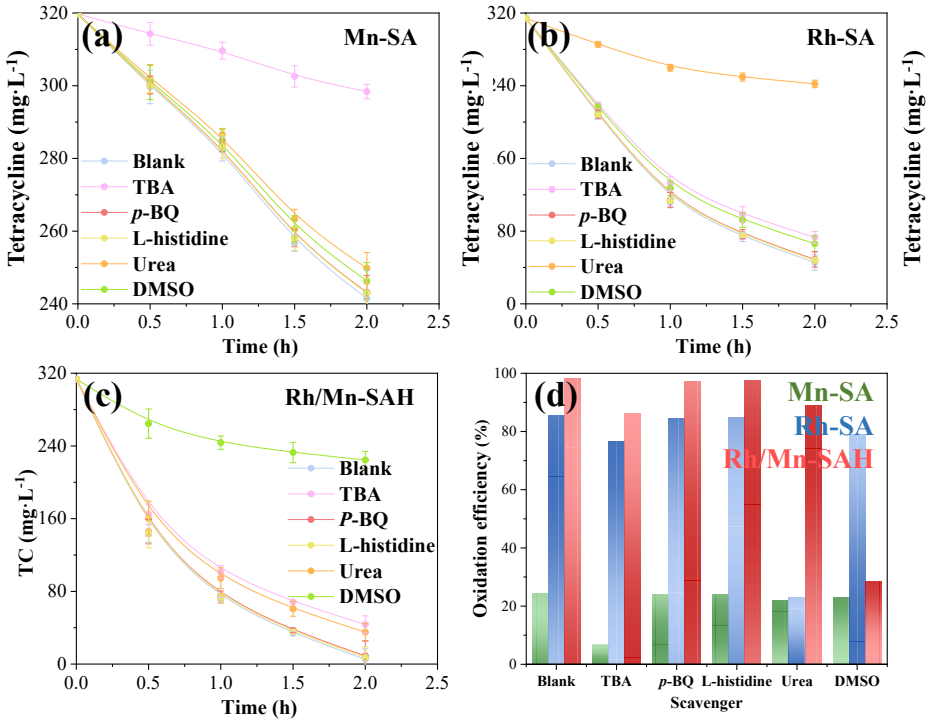

Figure S17. Tetracycline degradation under the presence of various scavengers for (a) Mn-SA, (b) Rh-SA, (c) Rh/Mn-SAH, and (d) calculated oxidation efficiency. Experimental conditions: initial tetracycline concentration = 320 mg·L^{-1}, initial NaCl concentration = 60 mM, current density = 20 mA·cm^{-2}.

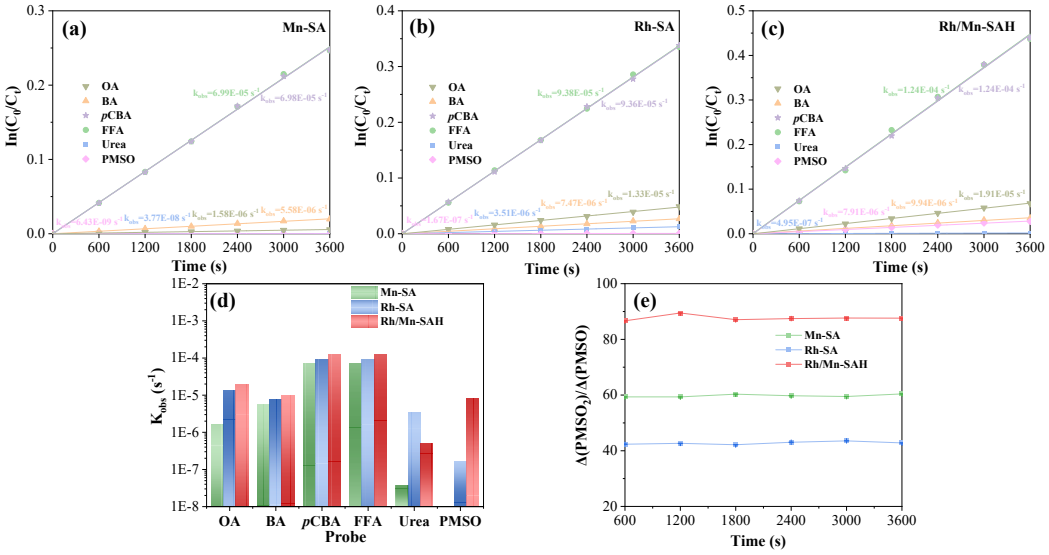

Figure S18. The pseudo-first-order kinetics of probe oxidation for (a) Mn-SA, (b) Rh-SA, and (c) Rh/Mn-SAH. (d) The measured k_{obs} for probe oxidation. (e) The conversion rate of PMSO toward $PMSO_2$..

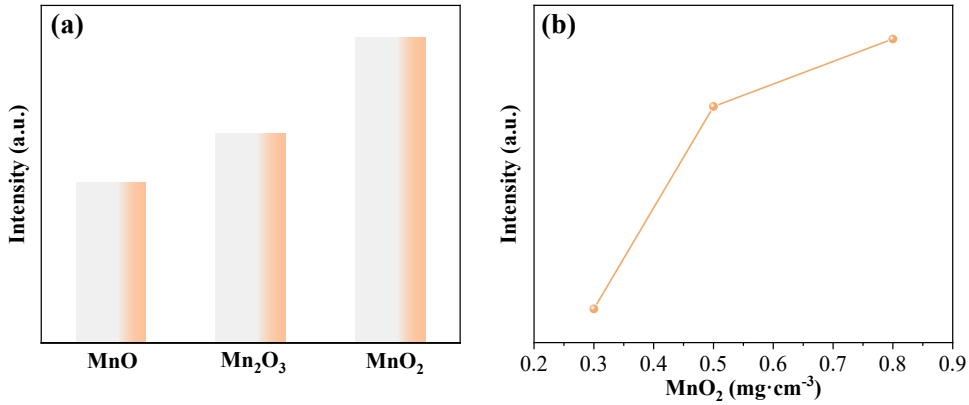

Figure S19. (a) Correlation between DMPOX EPR signal and compounds with different valences of Mn (b) Correlation between DMPOX EPR signal and MnO_2 dosage.

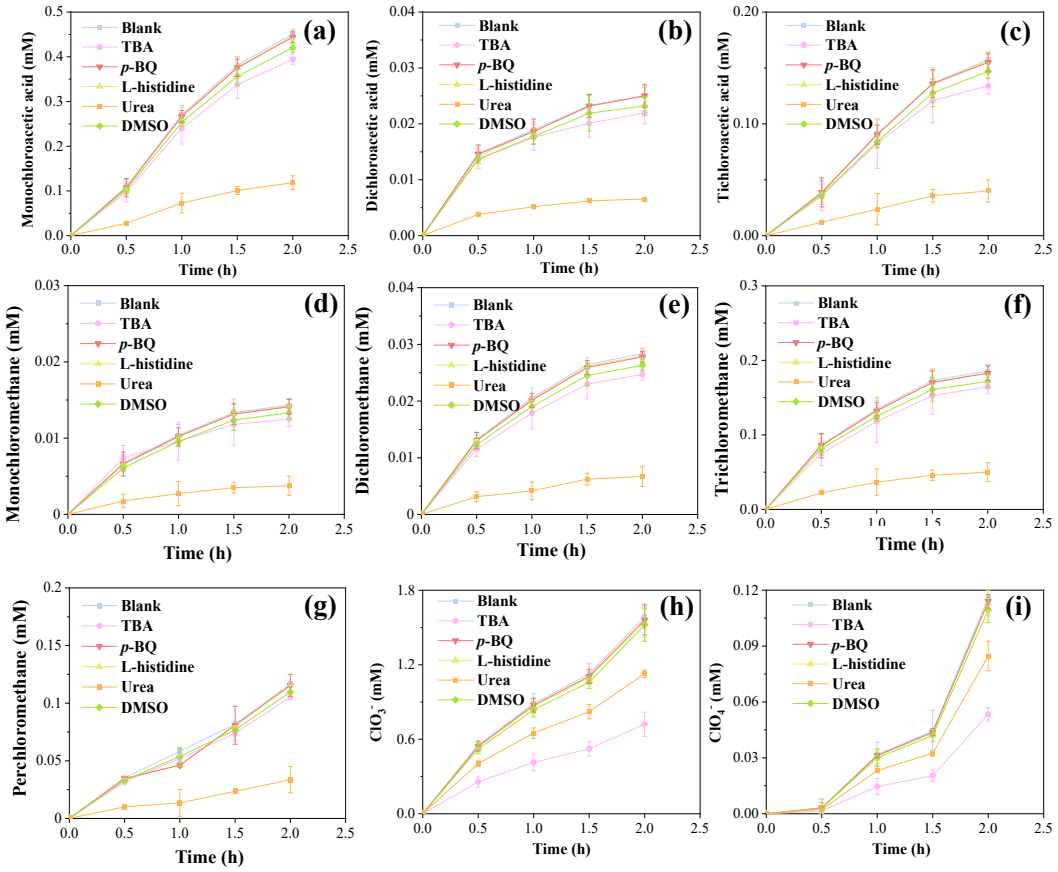

Figure S20. Chlorinated byproduct generation under the presence of various scavengers. (a) Monochloroacetic acid, (b) dichloroacetic acid, (c) trichloroacetic acid, (d) monochloromethane, (e) dichloromethane, (f) trichloromethane, (g) perchloromethane, (h) ClO_3^-, and (i) ClO_4^-. Experimental conditions: initial tetracycline concentration = 320 mg·L^{-1}, initial NaCl concentration = 60 mM, current density = 20 mA·cm^{-2}.

Figure S21. Chlorine-free and chlorinated intermediates detected during electrocatalytic oxidation of tetracycline in Rh-SA.

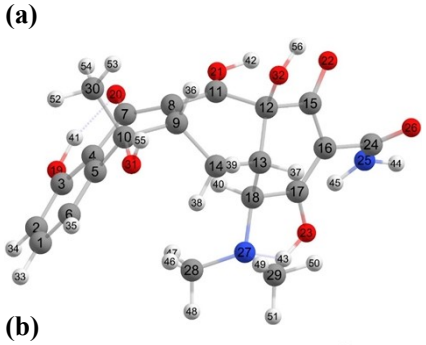

(c)

Atom	No	q(N)	q(N+1)	q(N-1)	f^-
C	1	-0.0278	-0.073	0.0097	0.038
C	2	-0.0595	-0.0853	-0.016	0.044
C	3	0.0874	0.066	0.133	0.046
C	4	-0.0452	-0.0509	-0.01	0.035
C	5	0.0031	-0.0141	0.0208	0.018
C	6	-0.0592	-0.0785	0.0091	0.068
C	7	0.1242	0.0698	0.133	0.009
C	8	-0.047	-0.0691	-0.0023	0.045
C	9	-0.0278	-0.0306	-0.0219	0.006
C	10	0.0865	0.0855	0.0875	0.001
C	11	0.0905	0.0464	0.13	0.039
C	12	0.0686	0.0589	0.0726	0.004
C	13	-0.0229	-0.0262	-0.0205	0.002
C	14	-0.0563	-0.0613	-0.0504	0.006
C	15	0.1292	0.0807	0.131	0.002
C	16	-0.0631	-0.0795	-0.0557	0.007
C	17	0.1073	0.0602	0.1116	0.004
C	18	0.0194	0.017	0.02	0.0007
O	19	-0.1947	-0.223	-0.1112	0.084
O	20	-0.2429	-0.3081	-0.2136	0.029
O	21	-0.1519	-0.1862	-0.1077	0.044
O	22	-0.2402	-0.3087	-0.216	0.024
O	23	-0.1594	-0.1991	-0.1433	0.016
C	24	0.1587	0.1554	0.1706	0.012
N	25	-0.1448	-0.156	-0.1277	0.017
O	26	-0.2979	-0.3227	-0.247	0.051
N	27	-0.0583	-0.0598	-0.0464	0.012
C	28	-0.0384	-0.042	-0.0342	0.004
C	29	-0.0373	-0.0433	-0.0302	0.007
C	30	-0.091	-0.0985	-0.0847	0.006
O	31	-0.2047	-0.2138	-0.1963	0.008
O	32	-0.2125	-0.2385	-0.1898	0.023

Figure S22. (a) Ball-and-stick model, (b) differential charge density, and (c) Fukui index of tetracycline molecule.

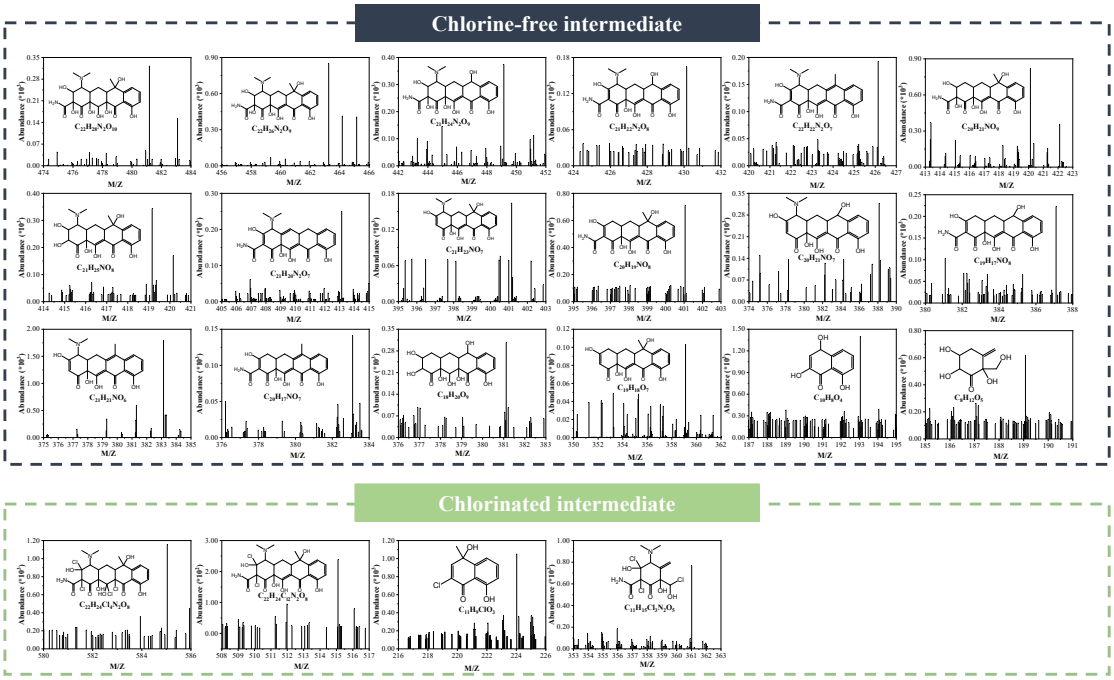

Figure S23. Chlorine-free and chlorinated intermediates detected during electrocatalytic oxidation of tetracycline in Rh/Mn-SAH.

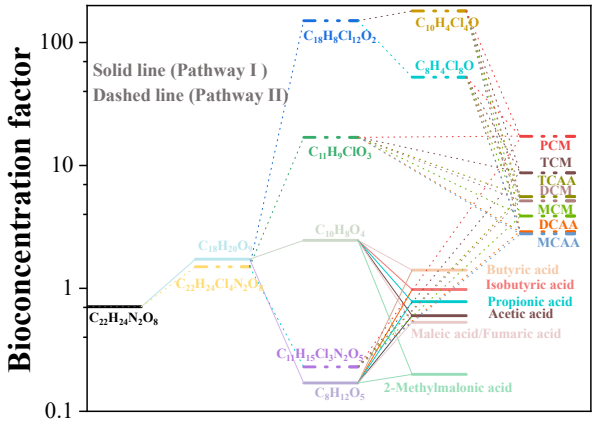

Figure S24. Bioconcentration factor of various degradation intermediates.

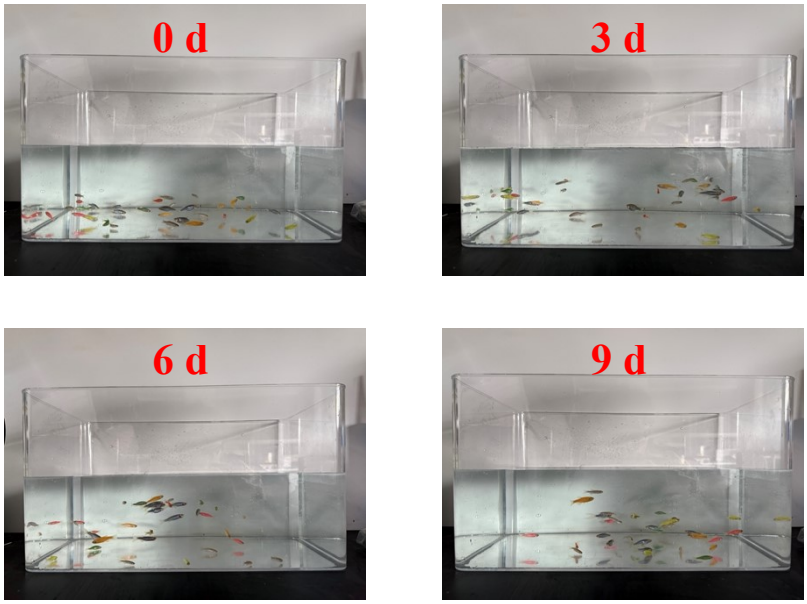

Figure 25. The viability of zebrafish in treated wastewater.

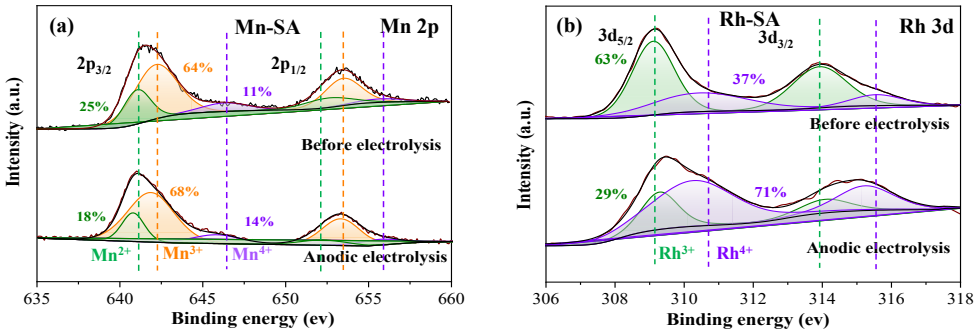

Figure S26. XPS spectra before electrolysis, and during anodic electrolysis in terms of (a) Mn 2p in Mn-SA and (b) Rh 3d in Rh-SA.

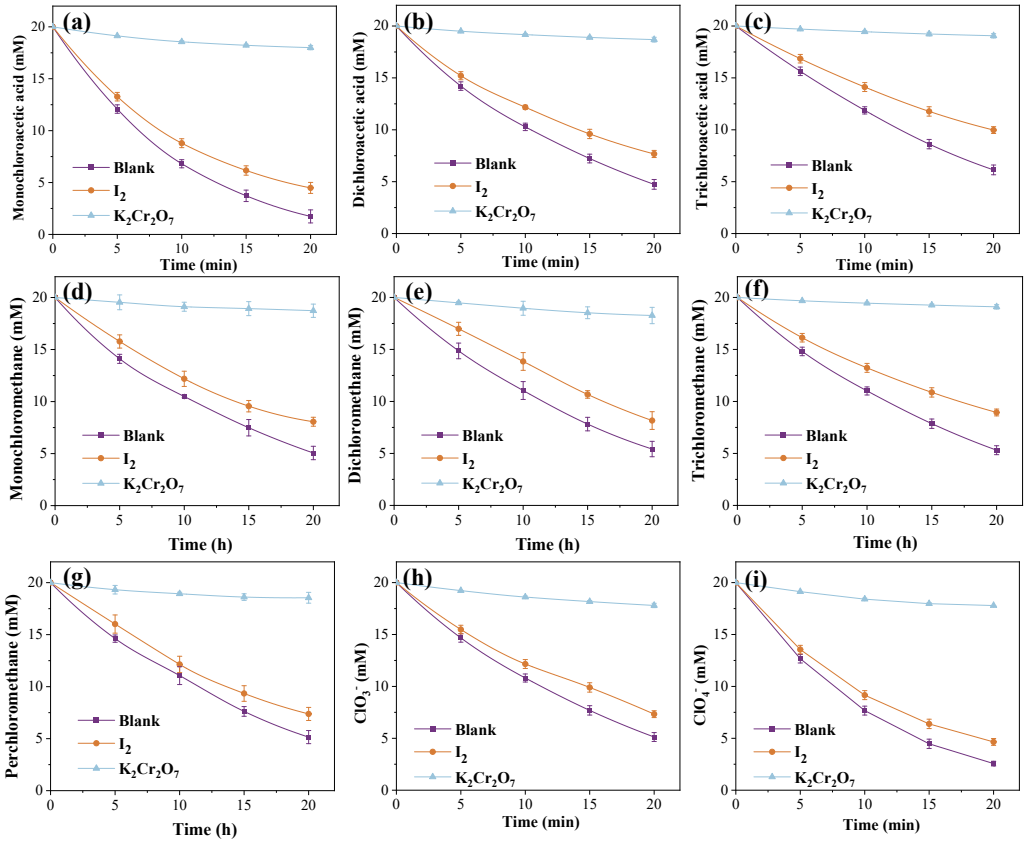

Figure S27. Chlorinated byproduct reduction under the presence of various scavengers. (a) Monochloroacetic acid, (b) dichloroacetic acid, (c) trichloroacetic acid, (d) monochloromethane, (e) dichloromethane, (f) trichloromethane, (g) perchloromethane, (h) ClO_3^-, and (i) ClO_4^-. Experimental conditions: initial chlorinated byproduct concentration = 20 mM, and current density = 20 mA·cm^{-2}.

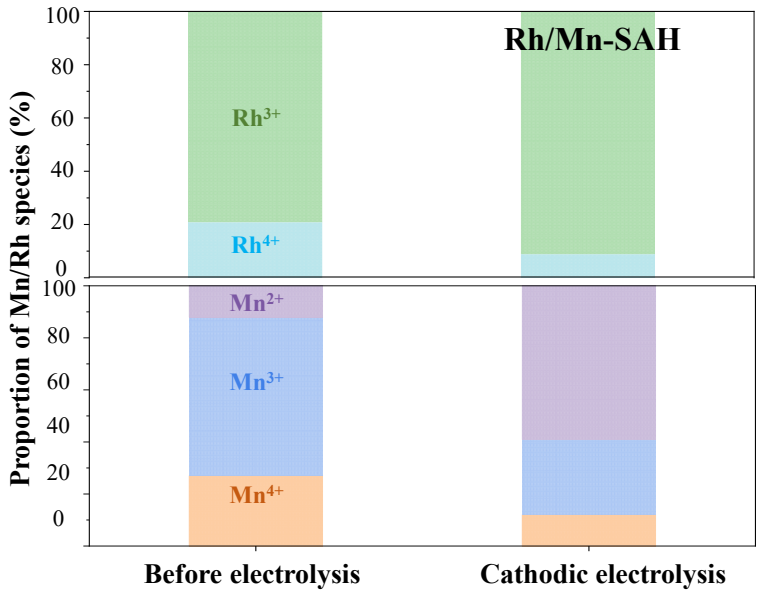

Figure S28. The relative proportion of Mn^{n+} and Rh^{n+} before electrolysis, and during cathodic electrolysis for Rh/Mn-SAH.

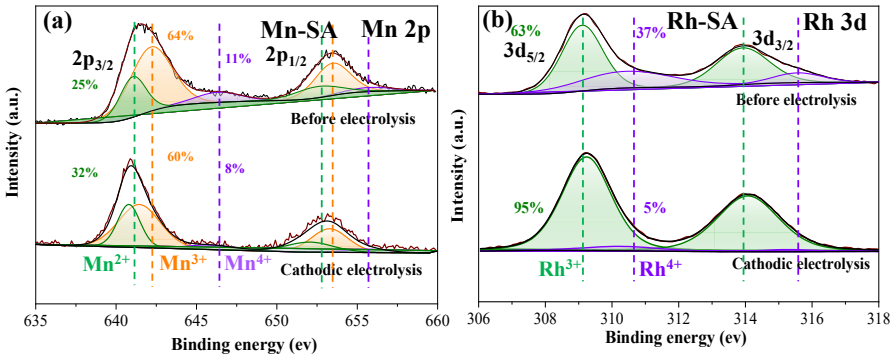

Figure S29. XPS spectra before electrolysis, and during cathodic electrolysis in terms of (a) Mn 2p in Mn-SA and (b) Rh 3d in Rh-SA.

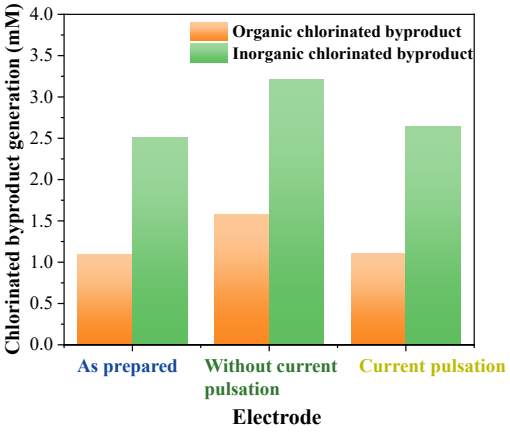

Figure S30. Chlorinated byproduct generation by Rh/Mn-SAH in as-prepared, without current pulsation, and with current pulsation conditions.

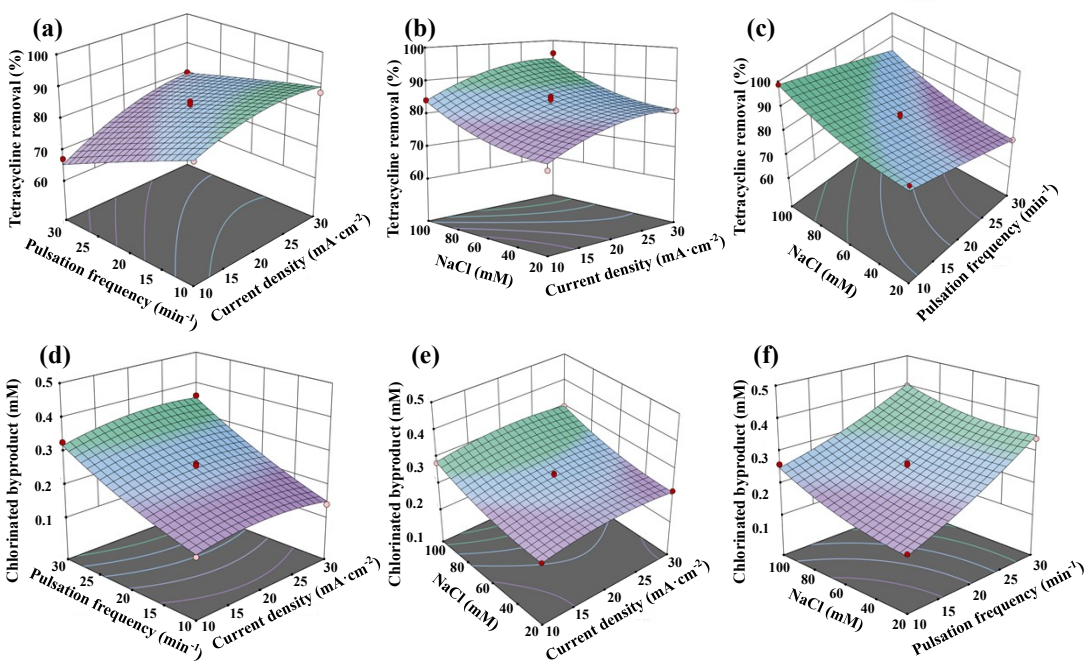

Figure S31. Response surfaces relating tetracycline degradation to (a) pulsation frequency and current density, (b) NaCl concentration and current density, and (c) NaCl concentration and pulsation frequency. Response surfaces relating chlorinated byproduct concentration to (d) pulsation frequency and current density, (e) NaCl concentration and current density, and (f) NaCl concentration and pulsation frequency.

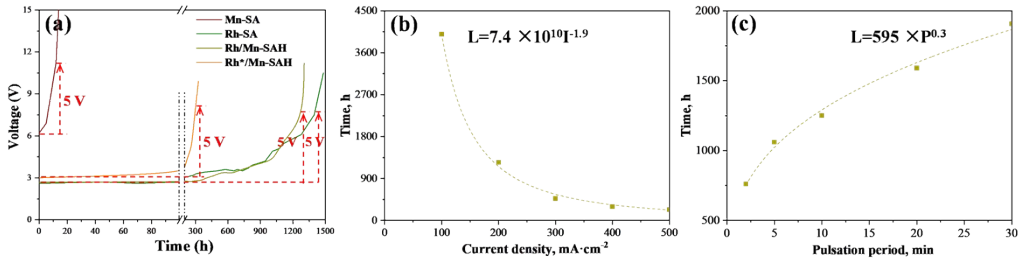

Figure S32. (a) Accelerated life test under a current density of 200 mA·cm^{-2} and a pulsation period of 5 min; (b) the dependence of lifespan on current density, and (c) the dependence of lifespan on pulsation period.

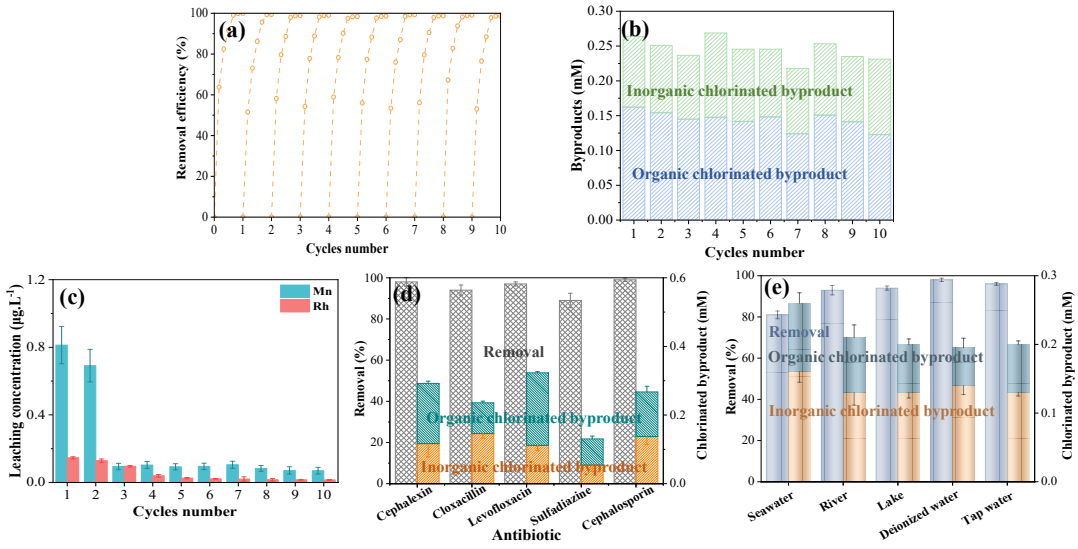

Figure S33. The operational durability of (a) tetracycline degradation, (b) chlorinated byproduct concentration, and (c) Mn/Rh leaching concentration. (d) The universal applicability of the electrode for cephalexin, cloxacillin, levofloxacin, sulfadiazine, and cephalosporin degradation. (e) The tetracycline degradation efficacy and byproduct generation under various water matrice. Experimental conditions: initial antibiotic concentration = 320 mg·L^{-1}, initial NaCl concentration = 60 mM, current

density = 20 $mA \cdot cm^{-2}$.

Table S1. The content of Rh and Mn elements in Mn-SA and Rh-SA detected by ICP-MS.

Catalysts	Rh (wt.%)	Mn (wt.%)
Rh-SA	0.08	/
Mn-SA	/	0.09

Table S2. The arrangements of the experiment in RSM.

Run	Current density (X_1), mA·cm^{-2}	Pulsation frequency (X_2), min^{-1}	NaCl concentration (X_3), mg·L^{-1}
1	20	10	100
2	20	20	60
3	20	20	60
4	20	10	20
5	20	20	60
6	10	20	100
7	20	30	100
8	30	20	20
9	30	30	60
10	10	10	60
11	20	30	20
12	10	20	20
13	30	10	60
14	20	20	60
15	30	20	100
16	20	20	60
17	10	30	60

Table S3. EXAFS fitting parameters at the Mn\Rh *K*-edges for various samples (S_0^2 = 0.85).

Sample	Shell	N^a	R(Å)^b	$\sigma^2 \times 10^3$(Å^2)^c	ΔE_0(eV)^d	R-factor
Mn_2O_3	Mn-O	2.2 ± 0.2	1.85 ± 0.02	2.6 ± 2.4	-6.22 ± 3.18	0.018
Mn-SA	Mn-O	2.5 ± 0.2	1.85 ± 0.01	2.6 ± 1.6	9.00 ± 0.19	0.014
Rh/Mn-SAH	Mn-O	5.6 ± 1.2	1.85 ± 0.02	7.3 ± 3.8	8.76 ± 1.73	0.015
MnO_2	Mn-O	5.4 ± 0.6	1.89 ± 0.01	3.1 ± 2.2	9.10 ± 0.36	0.016
Rh_2O_3	Rh-O	3.1 ± 0.9	1.99 ± 0.01	1.6 ± 3.6	-1.21 ± 3.12	0.018
Rh-SA	Rh-O	3.4 ± 0.6	1.99 ± 0.02	9.0 ± 1.4	4.52 ± 1.81	0.011
Rh/Mn-SAH	Rh-O	3.3 ± 0.6	1.99 ± 0.01	0.5 ± 2.7	0.47 ± 1.96	0.020

[a] N refers coordination numbers; [b] R refers bond distance; [c] σ^2 refers Debye-Waller factors; [d] ΔE_0 refers the inner potential correction. R factor refers goodness of fit.

Table S4. R_{ct} and W_{mt} obtained from EIS plots.

Anodes	R_{ct}[a] (Ω)	W_{mt}[b] (Ω)
Mn-SA	434 Ω	12.1 Ω
Rh-SA	2.38 Ω	6.91 Ω
Rh/Mn-SAH	3.79 Ω	7.79 Ω
Rh*/Mn-SAH	5.18 Ω	9.56 Ω

[a] R_{ct} refers to the charge transfer resistance, Ω. [b] W_{mt} refers to the mass transfer resistance, Ω.

Table S5. The second-order reaction rate constants between probe compounds or tetracycline with various oxidative species.

Probe compounds	$k_{\bullet OH}$ ($M^{-1}\cdot s^{-1}$)	k_{RCS} ($M^{-1}\cdot s^{-1}$)	$k_{^1O_2}$ ($M^{-1}\cdot s^{-1}$)	$k_{\bullet O_2^-}$ ($M^{-1}\cdot s^{-1}$)	$k_{MO_{X+1}}$ ($M^{-1}\cdot s^{-1}$)	Ref
Benzoic acid (BA)	1.20×10^9	N/A	No reaction	No reaction	No reaction	[4,5]
p-Chlorobenzoic acid (*p*CBA)	1.50×10^{10}	N/A	1.40×10^7	8.60×10^7	No reaction	[5-7]
Furfuryl alcohol (FFA)	1.50×10^{10}	N/A	1.20×10^8	3.50×10^3	No reaction	[7,8]
Methyl phenyl sulfoxide (PMSO)	3.61×10^9	N/A	N/A	N/A	2.00×10^6	[5,9]
Urea	N/A	1.0×0^7	N/A	N/A	N/A	[10]
Tetracycline	5.40×10^9	5.90×10^8	3.40×10^5	2.70×10^3	9.61×10^7	[11,12,13]

References

1 H. Jin, X. Xu, R. Liu, X. Wu, X. Chen, D. Chen, X. Zheng, M. Zhao and Y. Yu, *Water Res.*, 2024, **252**, 121229.

2 H. Jin, X. Xu, R. Liu, X. Wu, X. Chen, X. Zheng, M. Zhao and Y. Yu, *Chem. Eng. J.*, 2024, **483**, 149195.

3 H. Shi, Y. Wang, C. Li, R. Pierce, S. Gao and Q. Huang, *Environ. Sci. Technol.*, 2019, **53**, 14528-14537.

4 S. Liou and M. C. Dodd, *Water Res.*, 2021, **200**, 117142.

5 B. Liu, W. Guo, H. Wang, S. Zheng, Q. Si, Q. Zhao, H. Luo and N. Ren, *J. Hazard. Mater.*, 2021, **416**, 125679.

6 J. Cong, G. Wen, T. Huang, L. Deng and J. Ma, *Chem. Eng. J.*, 2015, **264**, 399-403.

7 Y. Guo, J. Long, J. Huang, G. Yu and Y. Wang, *Water Res.*, 2022, **215**, 118275.

8 L. Gao, Y. Guo, J. Zhan, G. Yu and Y. Wang, *Water Res.*, 2022, **221**, 118730.

9 Y. Zong, X. Guan, J. Xu, Y. Feng, Y. Mao, L. Xu, H. Chu and D. Wu, *Environ. Sci. Technol.*, 2020, **54**, 16231-16239.

10 Y. Yang, N. C. Ramos, J. A. Clark and H. W. Hillhouse, *Water Res.*, 2022, **221**, 118722.

11 A. Kladna, T. Michalska, P. Berczynski, I. Krukb and H. Y. Aboul-Enein, *Luminescence*, 2012, **27**, 249-255.

12 D. Guo, Y. Liu, H. Ji, C. Wang, B. Chen, C. Shen, F. Li, Y. Wang, P. Lu and W. Liu, *Environ. Sci. Technol.*, 2021, **55**, 4045-4053.

13 S. Lu, X. Li, Y. Cheng, J. Zhou and G. Zhang, *Proc. Natl. Acad. Sci. U.S.A.*, 2023, **120**, e1988132176.